

Time-domain observation of interlayer exciton formation and thermalization in a MoSe₂/WSe₂ heterostructure

Veronica R. Policht^{1,6*}, Henry Mittenzwey^{2*}, Oleg Dogadov¹, Manuel Katzer², Andrea Villa¹, Qiuyang Li³, Benjamin Kaiser⁴, Aaron M. Ross¹, Francesco Scotognella¹, Xiaoyang Zhu³, Andreas Knorr², Malte Selig², Giulio Cerullo^{1,5} and Stefano Dal Conte^{1*}

¹Department of Physics, Politecnico di Milano, Piazza Leonardo da Vinci 32, Milano, 20133, Italy.

²Institut für Theoretische Physik, Nichtlineare Optik und Quantenelektronik, Technische Universität Berlin, Hardenbergstraße 36, 10623, Berlin, Germany.

³Department of Chemistry, Columbia University, 3000 Broadway, New York, 10027, NY, United States.

⁴Zuse-Institut Berlin, Takustraße 7, 14195, Berlin, Germany.

⁵CNR-IFN, Piazza Leonardo da Vinci 32, Milano, 20133, Italy.

⁶Current Address: U.S. Naval Research Laboratory, 4555 Overlook Avenue SW, Washington, DC, 20375, USA.

*Corresponding author(s). E-mail(s): veronica.policht.ctr@nrl.navy.mil; h.mittenzwey@tu-berlin.de; stefano.dalconte@polimi.it;

Abstract

Vertical heterostructures (HS) of transition metal dichalcogenides (TMDs) host interlayer excitons (ILX), with electrons and holes residing in different layers. With respect to their intralayer counterparts, ILX feature much longer lifetimes and diffusion lengths, paving the way to excitonic optoelectronic devices operating at room temperature. While the recombination dynamics of ILX has been intensively studied, the formation process and its underlying physical mechanisms are still largely unexplored. Here we use ultrafast transient absorption spectroscopy with a white-light probe, spanning both intralayer and interlayer exciton resonances, to simultaneously capture and time-resolve interlayer charge transfer and ILX formation dynamics in a MoSe₂/WSe₂ HS. We find that the ILX formation timescale is nearly an order of magnitude (~ 1 ps) longer than the interlayer charge transfer time (~ 100 fs). Microscopic calculations attribute the relative delay to an interplay between a phonon-assisted interlayer exciton cascade and subsequent cooling processes, and excitonic wave-function overlap. Our results provide an explanation to the efficient photocurrent generation observed in optoelectronic devices based on TMD HS, as the ILX have an opportunity to dissociate during their thermalization process.

Keywords: 2D Materials, Interlayer Exciton, Transition Metal Dichalcogenide, Heterostructures

Introduction

Monolayer (ML) transition metal dichalcogenides (TMDs) exhibit remarkable physical properties which make them an ideal platform to study exciton physics and to realize novel optoelectronic devices [1]. The dimensional reduction from bulk to 2D results in the formation of strongly bound excitons due to increased quantum confinement and reduced Coulomb screening, along with spin-valley locking due to the inversion symmetry breaking [2, 3]. The

ability to vertically stack multiple TMDs, forming van der Waals heterostructures (HS) without lattice matching constraints, has dramatically increased recent interest in these materials [4]. Despite the fact that weak out-of-plane interactions largely preserve the electronic structures of each layer, stacked HS display novel properties and functionalities not present in constituent monolayers. HS with Type II band alignment, where the valence band maximum and the conduction band minimum are in different layers, can host interlayer excitons (ILX) (Fig. 1a) which arise following interlayer charge transfer (ICT) [5–7] and consist of spatially separated Coulomb-bound electron-hole states with binding energies up to 100s meV [8]. The ILX in TMD-HS is commonly detected via its photoluminescence (PL) in the near-infrared (NIR), below the energy of the optical gap of the two layers (Fig. 1b) [9–13]. The ILX is characterized by a long recombination time (up to hundreds of nanoseconds [14, 15]) and reduced oscillator strength (two orders of magnitude lower than that of intralayer excitons) due to the small spatial overlap of the electron and hole wave functions and, in some instances, their momentum-indirect character [9, 12, 16–18]. One of the most intriguing properties of TMD-HS is the lateral confinement of the ILX within moiré potentials, which are formed at small interlayer twist angles [13, 19–22].

ILX dynamics have been explored in different TMD-HS by time-resolved techniques [8]. The ILX recombination dynamics measured by time-resolved PL exhibit multiple decay components which exceed the recombination lifetimes of intralayer excitons by several orders of magnitude [9, 23]. The ILX relaxation dynamics have also been indirectly inferred from the photobleaching (PB) dynamics of intralayer excitons as measured by transient absorption (TA) optical spectroscopy [24]. On the other hand, the formation dynamics of the ILX are very difficult to access directly due to several factors, including the weak oscillator strength [25, 26] and the rapidity of the ICT process that leads to ILX formation, which typically ranges from tens to hundreds of femtoseconds [5–7, 24, 27, 28]. Time-resolved PL lacks the temporal resolution required to observe these processes. Attempts to resolve the transition from intralayer excitons to ILX have been done by measuring the formation of a novel $1s$ - $2p$ transition in the mid-IR range [29]. More recently, time- and angle-resolved photoemission spectroscopy (tr-ARPES) experiments have addressed ILX formation dynamics [30, 31] by probing the energy-momentum dispersion of photoexcited quasiparticles in real time and distinguishing excitons from single particle states according to their energy-momentum dispersion [31–36]. A recent tr-ARPES study [31] was able to track the ILX formation process following a phonon-assisted interlayer electron transfer as mediated by intermediate scattering to the Σ valleys. Despite the strengths of this technique, the limited energy resolution and the extremely low intensity of the photoemission signal above the Fermi level complicates the ability to disentangle ILX formation from ICT dynamics [37].

Here we use ultrafast optical TA spectroscopy to directly probe the transient optical response of the ILX in a MoSe₂/WSe₂ HS. These measurements are enabled by highly stable and broadband white light probe pulses spanning the visible to the NIR. The resulting high signal-to-noise measurements are capable of resolving the ILX formation dynamics through its weak TA signal (two orders of magnitude lower than the TA of the intralayer exciton) while simultaneously measuring intralayer exciton and interlayer hole transfer (IHT) dynamics. The ILX signal shows a delayed growth on a picosecond timescale, which is significantly longer than the experimentally

measured 100-fs IHT process from MoSe₂ to WSe₂. We simulate the exciton dynamics by solving the microscopic Heisenberg equations of motion and find that the difference in formation timescales is due to phonon-assisted hole tunneling of photo-excited excitons which gives rise to hot ILX populations that quickly exchange energy and momentum with phonons. The relaxation down to the ILX ground state proceeds through multiple scattering processes involving higher energy interlayer *s* states. Our simulations demonstrate that these hot ILX populations contribute strongly to the WSe₂ PB signal but only weakly to the optically bright ILX transition, resulting in the relative delay of the ILX signal as the populations cool.

Results

Experimental Results

Experiments are performed on a large-area (mm-scale) MoSe₂/WSe₂ HS fabricated using a gold tape exfoliation method (see details in Supplementary Note 1.1) [38]. The HS is prepared with a 4°, or nearly-aligned, interlayer twist angle, characterized using polarization-resolved second harmonic generation (Supplementary Fig. 1a). We focus on the 4° HS in the main manuscript, though experiments were also performed on a nearly anti-aligned MoSe₂/WSe₂ HS with twist angle of 57° (Supplementary Fig. 1b). HS prepared with small twist angles away from either aligned (0°) or anti-aligned (60°) have been shown to have strong ILX PL signals [11]. A clear signature of the ILX in the 4° HS is the low-energy peak in the PL spectrum at $\hbar\omega = 1.35$ eV (Fig. 1b) to the red of the intralayer PL peaks, which are quenched relative to the PL signals of the individual MLs (Supplementary Fig. 6). Both momentum-direct ($K - K$) and momentum-indirect ($\Sigma - K$) electron-hole transitions are expected to contribute to the PL of the ILX [9, 12, 16, 39] which can help to account for the width of the peak in Fig. 1b. We apply ultrafast TA spectroscopy with a broadband white-light continuum (WLC) probe to study the ILX formation dynamics. We selectively photoexcite the MoSe₂ layer by tuning a narrow-band (10 nm) 70-fs pump pulse on resonance with the A exciton peak of MoSe₂ ($\hbar\omega = 1.58$ eV) with a fluence of $3 \mu\text{J}/\text{cm}^2$ (Supplementary Fig. 2a). For simplicity, when discussing the experimental results, we adopt a notation for the intralayer A and B excitons of each layer using a subscript corresponding to the layer's transition metal (A_X and B_X where $X = \text{Mo}$ or W). The WLC probe beam is generated in a yttrium aluminium garnet (YAG) crystal pumped by a 1 eV pulse and spans a broad spectral window (1.2-2.3 eV) that includes both intralayer excitons and the ILX of the HS (Supplementary Fig. 2a). Unless otherwise stated, the pump and probe pulses are co-circularly polarized such that they access the ($K - K$) optical transitions.

Figure 2a reports a 2D map of the differential transmission ($\Delta T/T$) signal at 77 K as a function of pump-probe delay and probe photon energy. The spectrum is dominated by positive PB signals (red contours) at the energies of the intralayer excitons of both layers (i.e. A_{Mo} , A_W , B_{Mo} , B_W) with signal strengths on the order of $\Delta T/T \sim 10^{-2}$. The transient signal at the energy of A_{Mo} exciton displays an instantaneous (i.e. pulsewidth-limited) build-up and is the result of the interplay of multiple processes, including quenching of the exciton oscillator strength due to phase-space filling, energy renormalization, and lineshape broadening of the exciton resonance due to Coulomb

many-body effects [40]. The same formation dynamics are observed for the B_{Mo} resonance as a consequence of the exchange-driven mixing of the excitons in the $(K - K)$ valley [41] and light-induced reduction of the Coulomb screening, leading to an instantaneous renormalization of the exciton resonances [42]. Following excitation of the A_{Mo} exciton, the A_W resonance shows a delayed PB due to IHT from $MoSe_2$ to WSe_2 . The finite build-up time of the A_W PB signal (0.20 ± 0.06 ps, Fig. 2c) provides a direct estimate of the timescale of the hole scattering process, which is in good agreement with previous observations [24]. The B_W excitonic resonance shows the same delayed signal formation owing to coupling with the A_W exciton.

Focusing on the ILX energy region of the 2D $\Delta T/T$ map below the optical gap of the intralayer excitons, the TA spectrum at 4 ps pump-probe delay shows a broad peak with a signal strength $\Delta T/T \sim 10^{-4}$ (Fig. 2b). We confirm that this peak is unique to the HS through control measurements on isolated $MoSe_2$ and WSe_2 MLs (see Supplementary Note 2.4) and attribute it to PB of the ILX following IHT. The relative strengths of the TA signals of the intralayer excitons and of the ILX are in good agreement with the two orders of magnitude difference in the static transition dipole moments predicted by theory [43] and measured experimentally [25, 26]. Moreover, ILX exhibits valley circular dichroism as reported in Supplementary Note 2.5. We note that the ILX signature is peaked at slightly higher energy in the TA measurements compared to the ILX emission peak in Fig. 1. We attribute this energy mismatch to the fact that the optically bright ILX signal measured via TA is dominated by momentum-direct $(K - K)$ transitions [26] compared to the ILX PL signal which includes contributions from momentum-direct and momentum-indirect transitions [12, 17]. Figure 2c reports the formation dynamics of the ILX. Compared with the dynamics of A_{Mo} and A_W excitons (red and purple, respectively in Fig. 2c), the ILX TA signal (green) shows an remarkably slower formation timescale (800 ± 300 fs), significantly longer than the timescale of IHT (200 ± 60 fs). This behavior suggests that the optically-bright ILX does not form immediately upon IHT and that inferring ILX formation timescales from ICT signatures may be inadequate. The instantaneous peak in the ILX TA signal is due to the weak coherent artifact of the substrate during the pulse overlap, as confirmed by a control measurement on a blank substrate (see Supplementary Note 2.3). This weak coherent signal is not observed at A_W due to its much higher signal strength.

A recent ultrafast TA experiment performed with excitation densities above the exciton Mott transition reported the generation of an interlayer electron-hole plasma whose optical signature consisted of a broad photoinduced absorption (PIA) plateau extending below the optical gap of the HS [14]. The peak we observe at 1.37 eV is not related to this effect because (i) our excitation density is well below the Mott threshold and (ii) the ILX signal shows a positive signal consistent with a PB signature. At higher excitation densities, we find that the ILX PB signal persists while a negative PIA signal, related to pump-induced modification of the A_{Mo} excitonic resonance [42], increases in strength with fluence until it obscures the weak ILX signature (Supplementary Fig. 8).

Theoretical Model

To understand the observed delayed rise in the ILX signal compared to the IHT process, we developed a microscopic model [44, 45] for the exciton dynamics in a perfectly aligned (i.e. 0° twist angle) $MoSe_2/WSe_2$ HS. The binding

energies and the wavefunctions of both intra- and inter-layer excitons have been calculated as the solutions of the Wannier equation for the HS [46]. The effective Coulomb potential is determined by solving the Poisson equation for two dielectric slabs in three dielectric environments, following the procedure described in [47]. Our calculation includes both high energy bound exciton interlayer s states and unbound states above the band edge. A complete picture of the momentum-resolved formation and decay dynamics of excitons is achieved by solving the excitonic Bloch equations for the coherent excitonic polarization and the incoherent excitonic populations [48]. The pump-induced coherent excitonic polarization, P^{Mo} , obtained by excitation slightly above the A_{Mo} resonance, acts as a source term for the incoherent exciton populations via dephasing promoted by exciton-phonon scattering processes. Incoherent population contributions, $N^{Mo/W,\xi_e}$, are referred to with a superscript ξ corresponding to the valley location of the electron where $\xi_e = K/K'/\Sigma/\Sigma'$ while the hole remains in the K valley; the ILX population is similarly denoted as N^{IL,ξ_e} .

In Fig. 3a-d we report all the scattering processes leading to the formation of the incoherent excitonic populations included in our model. Intraband phonon scattering leads to a sudden decay of exciton polarization, P^{Mo} , and nearly instantaneous formation of an intravalley incoherent exciton population at the K valley of MoSe₂ layer, $N^{Mo,K}$ (Fig. 3a). Subsequent intervalley phonon-assisted electron scattering depletes the population, $N^{Mo,K}$, leading to the formation of intervalley excitons within the MoSe₂, $N^{Mo,K'/\Sigma/\Sigma'}$ (Fig. 3b). To reproduce the experimental results in Fig. 2 it is necessary to include the electron scattering to Σ/Σ' valleys which are located energetically near the K/K' valleys (Supplementary Fig. 4). Finally, interlayer phonon-assisted hole scattering proceeds to the K valley of WSe₂, resulting in the formation of momentum direct ILX populations, $N^{IL,K}$, and momentum indirect ILX populations, $N^{IL,K'/\Sigma/\Sigma'}$ with electrons located at the K or $K'/\Sigma/\Sigma'$ valleys in the MoSe₂ layer, respectively, and holes located at the K valley in the WSe₂ layer (Fig. 3c).

The differential transmission signals (DTS) (Eq. (2) in the Methods section) are calculated for the probe energies of A_{Mo} , (Eq. (6)), A_W (Eq. (7)), and the momentum-direct ILX (Eq. (8)) by performing a separation procedure of the excitonic Bloch equations regarding the probe and pump fields (Fig. 3d). The DTS temporal traces depend on the interplay of two factors. The first factor is the contribution of coherent polarization and incoherent excitonic populations (P^{Mo} , N^{Mo,ξ_e} and N^{IL,ξ_e}), where the electron and/or hole part of a given exciton population reduces the absorption of the corresponding optical transition by Pauli blocking and is thus responsible for a positive DTS signal. With this approach, PB signatures by electrons and/or holes are fully taken into account in the excitonic model. The second factor is given by the excitonic PB weights (Eq. 3 in the Methods section), which emerge as a consequence of the transformation into the excitonic basis and are displayed in Fig. 4b for the probed A_W and ILX transitions. Due to these PB weights, the overall excitonic populations do not determine the DTS timetraces directly but rather in a weighted fashion when summed over the center of mass (COM) momenta, \mathbf{Q} , and excitonic quantum numbers, μ , (Eq. (2)). We will examine the PB weights in more detail later on.

The calculated DTS time traces are reported in Fig. 3e together with the contributions of the individual excitonic populations (Fig. 3f-h). They qualitatively reproduce the experimental dynamics of intralayer excitons and the ILX, in particular their different formation timescales. The DTS of A_{Mo} exhibits a sharp rise followed

by a fast decay and a second delayed rise component (Fig. 3f). The sharp peak is mainly due to PB by the instantaneous coherent exciton polarization photoexcited at the K valley (pink line, Fig. 3f) and by the incoherent excitonic populations formed in the MoSe₂ layer following phonon-mediated dephasing (blue lines, Fig. 3). The second delayed rise component originates from the PB contribution of ILX populations (black line, Fig. 3f) which form following the decay of intralayer exciton populations via phonon-assisted hole tunneling. This bi-exponential behavior of the MoSe₂ of the HS is also present in the experimental transient optical response. A comparison of the TA signals, both measured and calculated, for the A_{Mo} exciton of an isolated ML and the HS (see Supplementary Fig. 12) confirms that the transient population of lower-energy ILX state strongly affects the dynamics of the intralayer A_{Mo} state. The DTS of A_W displays a longer formation time than for A_{Mo} as the signal is not influenced by the excitonic intralayer populations in MoSe₂ (Fig. 3g). Here, only the ILX populations arising from IHT contribute to the PB of the A_W signal.

The DTS of ILX shows similar behavior to the A_W but with a significantly longer risetime (Fig. 3h). We attribute this longer formation time to the relaxation dynamics of hot interlayer populations, represented schematically in Fig. 4a. Since the binding energies of the ILX (≈ 100 meV) are lower than the difference between the transition energies of A_{Mo} and ILX (≈ 300 meV), phonon-mediated hole transfer creates hot ILX populations, i.e. populations at high momenta \mathbf{Q} and/or higher energy bound and unbound s states of the Rydberg series (Fig. 4a), which subsequently scatter to lower-energy momenta and bound states via optical and acoustic phonons. The lower-energy bound states then slowly thermalize into a Boltzmann distribution via scattering with acoustic phonons with energies below the optical phonon bottleneck. Figure 4b reports the calculated momentum-dependent ILX occupations at different times, taking only the $1s$ state at the K valley into account as an example (the lowest energy parabola in Fig. 4a). The ILX occupation is initially peaked at higher momenta following IHT, after which phonon-assisted scattering processes gradually confine the ILX occupations to lower momenta.

This behavior along with the COM and quantum number dependent PB weights for ILX and A_W transitions (green and purple shaded areas, respectively in Fig. 4b) explains the physical origin of the relative delay in the PB signatures of the two transitions. The larger binding energy of the A_W exciton compared to the ILX leads to a broader PB weight distribution, as shown in Fig. 4b (see Supplementary Note 1.5). Probing the intralayer A_W transition is more sensitive to the overall excitonic occupation, whereas probing the ILX transition is mainly sensitive to the low-momenta states which are reached at longer delay times. Consequently, only the cold and lowest-energy bound ILX populations significantly contribute to the DTS signal of the ILX transition in Fig. 3h and the delayed risetime of the ILX compared to the A_W is related to the thermalization of the hot ILX populations. By directly comparing the DTS signals of the probed A_W and ILX transitions, we are able to trace the microscopic mechanisms of the ILX formation and relaxation processes.

Discussion

We have used TA spectroscopy with a combination of high sensitivity and broad spectral coverage to directly track the formation dynamics of ILX in a TMD HS. We find that ILX PB signal rises on a picosecond timescale,

significantly slower than the build-up dynamics of intralayer exciton PB signals in general and of IHT specifically. Microscopic calculations reproduce the experimental transient signals and explain the formation timescale in terms of different contributions. The hundreds of femtoseconds build-up time of the WSe₂ PB signal is mainly related to interlayer scattering of hot holes and therefore represents a rather direct estimation of the hot carrier injection process between the TMD layers of the HS. The slower rise time of the ILX signal is the result of the combination of two scattering processes: (1) phonon-mediated exciton cascade process from unbound and/or higher energy excitonic *s* states to the ground state and (2) intra-exciton energy and momentum relaxation of hot ILX populations. Our simulations also demonstrate that the dynamics of optically bright intra- and inter-layer excitons are influenced by optically dark momentum-indirect excitons.

Besides its fundamental interest, the delayed ILX formation observed and discussed here could explain a long-standing puzzle in optoelectronic devices based on TMD HS, namely the observation of efficient generation of photocurrent despite the large binding energy of the ILX [49–53]. During their several-hundred femtosecond thermalization process, in fact, the hot ILX have an opportunity to dissociate and form free charge carriers. We foresee that our combined theoretical-experimental approach can be extended to study in real-time exciton formation process in other systems, such as hybrid organic/TMD HS [54] and mixed dimensional van der Waals HS [55].

Methods

Sample Preparation

Large-area MoSe₂/WSe₂ HS are prepared using a modified gold tape exfoliation method [38] resulting in mm-scale ML flakes deposited onto 200 μm thick transparent SiO₂ substrates. TMD HS with varying twist angles are prepared and characterized using polarization-resolved second harmonic generation (Supplementary Fig. 1). We have mainly reported the static and time-domain measurements on a nearly-aligned HS with a 4° twist angle. Similar measurements were performed on a nearly-anti-aligned HS characterized by 57° twist angle (Supplementary Fig. 14). The HS are prepared with unoverlapped regions where the individual ML can be accessed for control measurements.

Transient Absorption Spectroscopy

Time-resolved and static optical measurements are performed at 77 K. TA spectroscopy measurements are performed in a transmission geometry (Supplementary Fig. 2b) with pump and probe beam diameters of 200 μm and 100 μm at the sample surface, respectively. The relatively large sample region accessed in these TA experiments represents a sort of ensemble measurement where sample heterogeneity contributes to the inhomogeneous broadening, as seen previously on similar samples [6]. The delay dependent $\Delta T/T$ map and spectra in Fig. 2a & b are measured by dispersing the transmitted broadband probe and acquiring it with a fast silicon spectrometer (Entwicklungsbuero EB Stresing) working at 1 kHz laser repetition rate. The probe pulse is a WLC generated

by focusing the output of a homemade NIR Optical Parametric Amplifier (OPA) centered at 1 eV into a YAG plate; the WLC spectrum extends from 1.2 to 2.3 eV, covering A/B intralayer and ILX of the HS (Supplementary Fig. 2a). The NIR OPA is seeded with a regeneratively amplified Ti-sapphire laser (Coherent, Libra) emitting 100-fs pulses at 1.55 eV and at a repetition rate of 1 kHz. The pump pulse is generated by a narrowband OPA tuned to the A_{Mo} excitonic resonance ($\hbar\omega = 1.59$ eV) and modulated at half the repetition rate of the laser. The temporal dynamics of the excitonic resonances (Fig. 2c) are measured by a different TA optical setup based on a Yb:KGW regenerative amplifier (Pharos, Light Conversion) providing 200-fs pulses at 1.2 eV and at a higher repetition rate of 100 kHz. The pump pulse is generated by the second harmonic of a near-IR OPA [56] tuned to the same energy and fluence conditions as experiments performed on the lower repetition rate TA setup. The WLC is generated by focusing the fundamental of the laser into a YAG crystal. The transmitted probe beam is then sent to a monochromator and a photodiode for lock-in detection. The pump is modulated by a Pockels cell to 50 kHz allowing to reach higher signal-to-noise ratio with respect to the 1 kHz system. The rise times of the TA signals are estimated by fitting the time traces with a rising exponential convoluted with a Gaussian function with full width at half maximum of the instrument response function (FWHM-IRF) of the respective TA setup. The estimated FWHM-IRF is 140 fs for both TA instruments.

Theoretical Calculations

To obtain the DTS theoretically, we solve the Bloch equations for the excitonic transitions $P_{\mu,\mathbf{Q}}^i = \langle \hat{P}_{\mu,\mathbf{Q}}^i \rangle$ up to third order in the electric field as in [44]. Here, $\hat{P}_{\mu,\mathbf{Q}}^i$ are the excitonic operators [45] carrying excitonic radial quantum number μ , center of mass momentum \mathbf{Q} and compound layer and valley index $i = \{l_h, \xi_h, l_e, \xi_e\}$ with electron/hole layer $l_{e/h} = M/W$ for MoSe₂ and WSe₂, electron valley index $\xi_e = K/K'/\Sigma/\Sigma'$ and hole valley index $\xi_h = K$. Performing a linearization in the weak probe pulse limit [57], we are able to separate the pump induced coherent polarizations $P_{\mu,\mathbf{Q}}^i$ and incoherent populations

$$N_{\mu,\mathbf{Q}}^i = \langle \hat{P}_{\mu,\mathbf{Q}}^{\dagger,i} \hat{P}_{\mu,\mathbf{Q}}^i \rangle_c \quad (1)$$

from the probe-induced dynamics. The coupled equations of motion [48] are then solved in the time domain. The hole tunneling process is implemented as in [46]. The subscript c in Eq. (1) accounts for the purely correlated (or incoherent) part of the expectation value in the spirit of [48, 58]. By assuming a Dirac delta-shaped probe pulse, we find an expression for the probe- and pump-induced macroscopic polarization $\mathbf{P}^i = \frac{1}{A} \sum_{\mu} \mathbf{d}_{\mu}^i P_{\mu,\mathbf{Q}=\mathbf{0}}^i$ which couples to Maxwell's equations giving the total electric field and therefore the transmission at the HS as in [59, 60]. Here, \mathbf{d}_{μ}^i is the excitonic dipole moment and A is the illuminated area of the sample. The DTS is then given by subtracting the transmission T^t of the probe pulse without pump pulse from the transmission T^{t+p} of the probe pulse with pump pulse: $\Delta T(\omega, \tau) = T^{t+p}(\omega, \tau) - T^t(\omega)$ [61]. In our case, since we are only interested in timetraces, we neglect Coulomb renormalization and nonlinear broadening [62] and focus solely on the Pauli-blocking induced PB dynamics, so that the DTS signal dependent on the time delay τ between pump and probe

pulses can be expressed as

$$\Delta T_{\mu}^i(\tau) \sim \sum_{i', \mathbf{Q}, \mu} \left(D_{\mathbf{Q}, \mu, \nu}^{e, i, i'} + D_{\mathbf{Q}, \mu, \nu}^{h, i, i'} \right) \left(|P_{\nu, \mathbf{Q}}^{i'}(\tau)|^2 \delta_{\mathbf{Q}, \mathbf{0}} + N_{\nu, \mathbf{Q}}^{i'}(\tau) \right), \quad (2)$$

where the matrix elements are given by

$$D_{\mathbf{Q}, \mu, \nu}^{e/h, i, i'} = \sum_{\mathbf{q}} \mathbf{d}_{\mu}^i \cdot \mathbf{d}_{\mathbf{q}}^{cv, i} \varphi_{\mu, \mathbf{q}}^{*, i} \varphi_{\nu, \mathbf{q} + (-\alpha_{i'}) / (+\beta_{i'}) \mathbf{Q}}^{*, i'} \varphi_{\nu, \mathbf{q} + (-\alpha_{i'}) / (+\beta_{i'}) \mathbf{Q}}^{i'} \delta_{\ell_{h/e}, \ell'_{h/e}} \delta_{\xi_{h/e}, \xi'_{h/e}}. \quad (3)$$

Here, $\mathbf{d}_{\mu}^i = \sum_{\mathbf{q}} \varphi_{\mu, \mathbf{q}}^i \mathbf{d}_{\mathbf{q}}^{*, cv, i}$ are the excitonic and $\mathbf{d}_{\mathbf{q}}^{cv, i}$ the electronic dipole moments, $\varphi_{\mu, \mathbf{q}}^i$ are the excitonic wave functions obtained by solving the Wannier equation for the respective excitonic configuration i with radial quantum number μ and relative momentum \mathbf{q} . α_i and β_i are the ratios of the effective masses [63]. In Eq. (3), the indices μ and i refer to the optically bright probed transition, whereas ν and i' reflect the bright as well as dark excitonic populations responsible for the Pauli blocking. These matrix elements can be viewed as convolutions in momentum space of the excitonic wave functions $\varphi_{\mu, \mathbf{q}}^i$ of the probed transitions i with the excitonic wave functions $\varphi_{\nu, \mathbf{q}}^{i'}$ of the pumped populations i' and constitute the crucial part of the explanation regarding the different DTS risetimes of the A_W and ILX transition as described in the Results section. The Wannier equation is solved for a HS using a Coulomb potential for two dielectric slabs in three dielectric environments, $\epsilon_1 = 3.9$ (SiO_2 substrate on the MoSe_2 side), $\epsilon_g = 1$ (assuming a vacuum environment between the layers) and $\epsilon_2 = 1$ (vacuum on the WSe_2 side), as in [47].

In the following, and to be in line with the notation used in the main part of the manuscript, we denote the excitonic populations under consideration as:

$$N^{Mo, \xi_e} = N^{M, K, M, \xi_e}, \quad N^{IL, \xi_e} = N^{W, K, M, \xi_e}, \quad (4)$$

and the excitonic coherent polarizations as:

$$P^{Mo} = P_{1s}^{M, K, M, K}, \quad P^W = P_{1s}^{W, K, W, K}, \quad P^{IL} = P_{1s}^{W, K, M, K}. \quad (5)$$

Therefore, the DTS signal for the probed A_{Mo} transition reads explicitly:

$$\begin{aligned} \Delta T^{A_{Mo}}(\tau) \sim & \sum_{\mathbf{Q}} \left(D_{\mathbf{Q}, 1s, 1s}^{e+h, Mo, K, Mo, K} \left(|P^{Mo}(\tau)|^2 \delta_{\mathbf{Q}, \mathbf{0}} + N_{\mathbf{Q}, 1s}^{Mo, K}(\tau) \right) \right. \\ & \left. + \sum_{\xi_e \neq K} D_{\mathbf{Q}, 1s, 1s}^{h, Mo, K, Mo, \xi_e} N_{\mathbf{Q}, 1s}^{Mo, \xi_e}(\tau) + \sum_{\mu} D_{\mathbf{Q}, 1s, \mu}^{e, Mo, K, IL, K} N_{\mathbf{Q}, \mu}^{IL, K}(\tau) \right), \end{aligned} \quad (6)$$

for the probed A_W transition we obtain:

$$\Delta T^{A_W}(\tau) \sim \sum_{\mathbf{Q}, \mu, \xi_e} D_{\mathbf{Q}, 1s, \mu}^{h, W, K, IL, \xi_e} N_{\mu, \mathbf{Q}}^{IL, \xi_e}(\tau), \quad (7)$$

and for the probed ILX transition it reads:

$$\begin{aligned} \Delta T^{ILX}(\tau) \sim \sum_{\mathbf{Q}} \left(D_{\mathbf{Q}, 1s, 1s}^{e, IL, K, Mo, K} \left(|P^{Mo}(\tau)|^2 \delta_{\mathbf{Q}, \mathbf{0}} + N_{1s, \mathbf{Q}}^{Mo, K}(\tau) \right) \right. \\ \left. + \sum_{\mu} D_{\mathbf{Q}, 1s, \mu}^{e+h, IL, K, IL, K} N_{\mu, \mathbf{Q}}^{IL, K}(\tau) + \sum_{\mu, \xi_e \neq K} D_{\mathbf{Q}, 1s, \mu}^{h, IL, K, IL, \xi_e} N_{\mu, \mathbf{Q}}^{IL, \xi_e}(\tau) \right). \end{aligned} \quad (8)$$

Eq. (6) displays the contribution of the probed A_{Mo} transition (red ellipse in Fig. 3d) with Pauli blocking due to electron and hole of the pumped momentum-direct excitonic transitions P^{Mo} and populations $N^{Mo, K}$ (first two terms) as well as due to the blocking of the hole of momentum-indirect excitonic populations $N^{Mo, K'/\Sigma/\Sigma'}$ (third term) and blocking of the electron of momentum-direct interlayer populations $N^{IL, K}$ (last term). Eq. (7) describes the probed A_W transition (purple ellipse in Fig. 3d) with Pauli blocking contributions due to holes of all four possible interlayer populations N^{IL, ξ_e} . Eq. (8) shows the probed ILX transition (green ellipse in Fig. 3d), where the first two terms account for Pauli blocking due to the electron of the pumped momentum-direct excitonic transitions P^{Mo} and populations $N^{Mo, K}$, the third term accounts for the blocking of electron and hole of the momentum-direct interlayer population $N^{IL, K}$, whereas the last term shows the contribution of the PB by the hole of the other momentum-indirect interlayer populations $N^{IL, K'/\Sigma/\Sigma'}$. All Pauli blocking terms feature distinctive momentum- and excitonic quantum number-dependent PB weights $D_{\mathbf{Q}, \mu, \nu}^{e/h, i, i'}$, which are given in Eq. (3).

References

- [1] Wang, Q. H., Kalantar-Zadeh, K., Kis, A., Coleman, J. N. & Strano, M. S. Electronics and optoelectronics of two-dimensional transition metal dichalcogenides. *Nature Nanotechnology* **7** (11), 699–712 (2012) .
- [2] Qiu, D. Y., da Jornada, F. H. & Louie, S. G. Optical Spectrum of MoS2: Many-Body Effects and Diversity of Exciton States. *Physical Review Letters* **111** (21), 216805 (2013) .
- [3] Schaibley, J. R. *et al.* Valleytronics in 2D materials. *Nature Reviews Materials* **1** (11), 16055 (2016) .
- [4] Geim, A. K. & Grigorieva, I. V. Van der Waals heterostructures. *Nature* **499** (7459), 419–425 (2013) .
- [5] Hong, X. *et al.* Ultrafast charge transfer in atomically thin MoS2/WS2 heterostructures. *Nature Nanotechnology* **9** (9), 682–686 (2014) .
- [6] Policht, V. R. *et al.* Dissecting Interlayer Hole and Electron Transfer in Transition Metal Dichalcogenide Heterostructures via Two-Dimensional Electronic Spectroscopy. *Nano Letters* **21** (11), 4738–4743 (2021) .

- [7] Purz, T. L. *et al.* Coherent exciton-exciton interactions and exciton dynamics in a MoSe₂/WSe₂ heterostructure. *Physical Review B* **104** (24), 1–6 (2021) .
- [8] Jiang, Y., Chen, S., Zheng, W., Zheng, B. & Pan, A. Interlayer exciton formation, relaxation, and transport in TMD van der Waals heterostructures. *Light: Science and Applications* **10** (1), 1–29 (2021) .
- [9] Rivera, P. *et al.* Observation of long-lived interlayer excitons in monolayer MoSe₂-WSe₂ heterostructures. *Nature Communications* **6** (1), 6242 (2015) .
- [10] Nagler, P. *et al.* Giant magnetic splitting inducing near-unity valley polarization in van der Waals heterostructures. *Nature Communications* **8** (1), 1–6 (2017) .
- [11] Nayak, P. K. *et al.* Probing Evolution of Twist-Angle-Dependent Interlayer Excitons in MoSe₂/WSe₂ van der Waals Heterostructures. *ACS Nano* **11** (4), 4041–4050 (2017) .
- [12] Hanbicki, A. T. *et al.* Double Indirect Interlayer Exciton in a MoSe₂/WSe₂ van der Waals Heterostructure. *ACS Nano* **12** (5), 4719–4726 (2018) .
- [13] Tran, K. *et al.* Evidence for moiré excitons in van der Waals heterostructures. *Nature* **567** (7746), 71–75 (2019) .
- [14] Wang, J. *et al.* Optical generation of high carrier densities in 2D semiconductor heterobilayers. *Science Advances* **5** (9), 2–10 (2019) .
- [15] Jauregui, L. A. *et al.* Electrical control of interlayer exciton dynamics in atomically thin heterostructures. *Science* **366** (6467), 870–875 (2019) .
- [16] Miller, B. *et al.* Long-Lived Direct and Indirect Interlayer Excitons in van der Waals Heterostructures. *Nano Letters* **17** (9), 5229–5237 (2017) .
- [17] Okada, M. *et al.* Direct and Indirect Interlayer Excitons in a van der Waals Heterostructure of hBN/WS₂/MoS₂/hBN. *ACS Nano* **12** (3), 2498–2505 (2018) .
- [18] Kunstmann, J. *et al.* Momentum-space indirect interlayer excitons in transition-metal dichalcogenide van der Waals heterostructures. *Nature Physics* **14** (8), 801–805 (2018) .
- [19] Jin, C. *et al.* Observation of moiré excitons in WSe₂/WS₂ heterostructure superlattices. *Nature* **567** (7746), 76–80 (2019) .
- [20] Alexeev, E. M. *et al.* Resonantly hybridized excitons in moiré superlattices in van der Waals heterostructures. *Nature* **567** (7746), 81–86 (2019) .

- [21] Seyler, K. L. *et al.* Signatures of moiré-trapped valley excitons in MoSe₂/WSe₂ heterobilayers. *Nature* **567** (7746), 66–70 (2019) .
- [22] Huang, D., Choi, J., Shih, C. K. & Li, X. Excitons in semiconductor moiré superlattices. *Nature Nanotechnology* **17** (3), 227–238 (2022) .
- [23] Nagler, P. *et al.* Interlayer exciton dynamics in a dichalcogenide monolayer heterostructure. *2D Materials* **4** (2), 025112 (2017) .
- [24] Wang, Z. *et al.* Phonon-Mediated Interlayer Charge Separation and Recombination in a MoSe₂/WSe₂ Heterostructure. *Nano Letters* **21** (5), 2165–2173 (2021) .
- [25] Ross, J. S. *et al.* Interlayer Exciton Optoelectronics in a 2D Heterostructure p-n Junction. *Nano Letters* **17** (2), 638–643 (2017) .
- [26] Barré, E. *et al.* Optical absorption of interlayer excitons in transition-metal dichalcogenide heterostructures. *Science* **376** (6591), 406–410 (2022) .
- [27] Liu, F., Li, Q. & Zhu, X. Direct determination of momentum-resolved electron transfer in the photoexcited van der Waals heterobilayer WS₂/MoS₂. *Physical Review B* **101** (20), 201405 (2020) .
- [28] Zimmermann, J. E. *et al.* Ultrafast Charge-Transfer Dynamics in Twisted MoS₂/WSe₂ Heterostructures. *ACS Nano* **15** (9), 14725–14731 (2021) .
- [29] Merkl, P. *et al.* Ultrafast transition between exciton phases in van der Waals heterostructures. *Nature Materials* **18** (7), 691–696 (2019) .
- [30] Karni, O. *et al.* Structure of the moiré exciton captured by imaging its electron and hole. *Nature* **603** (7900), 247–252 (2022) .
- [31] Schmitt, D. *et al.* Formation of moiré interlayer excitons in space and time. *Nature* **608** (7923), 499–503 (2022) .
- [32] Perfetto, E., Sangalli, D., Marini, A. & Stefanucci, G. First-principles approach to excitons in time-resolved and angle-resolved photoemission spectra. *Physical Review B* **94** (24), 245303 (2016) .
- [33] Rustagi, A. & Kemper, A. F. Photoemission signature of excitons. *Physical Review B* **97** (23), 1–7 (2018) .
- [34] Christiansen, D., Selig, M., Malic, E., Ernstorfer, R. & Knorr, A. Theory of exciton dynamics in time-resolved ARPES: Intra- and intervalley scattering in two-dimensional semiconductors. *Physical Review B* **100** (20), 205401 (2019) .

- [35] Dong, S. *et al.* Direct measurement of key exciton properties: Energy, dynamics, and spatial distribution of the wave function. *Natural Sciences* **1** (1), 1–8 (2021) .
- [36] Man, M. K. L. *et al.* Experimental measurement of the intrinsic excitonic wave function. *Science Advances* **7** (17), 1–7 (2021) .
- [37] Lee, W. *et al.* Time-resolved ARPES Determination of a Quasi-Particle Band Gap and Hot Electron Dynamics in Monolayer MoS₂. *Nano Letters* **21** (17), 7363–7370 (2021) .
- [38] Liu, F. *et al.* Disassembling 2D van der Waals crystals into macroscopic monolayers and reassembling into artificial lattices. *Science* **367** (6480), 903–906 (2020) .
- [39] Rivera, P. *et al.* Interlayer valley excitons in heterobilayers of transition metal dichalcogenides. *Nature Nanotechnology* **13** (11), 1004–1015 (2018) .
- [40] Trovatiello, C. *et al.* Disentangling Many-Body Effects in the Coherent Optical Response of 2D Semiconductors. *Nano Letters* **22** (13), 5322–5329 (2022) .
- [41] Guo, L. *et al.* Exchange-driven intravalley mixing of excitons in monolayer transition metal dichalcogenides. *Nature Physics* **15** (3), 228–232 (2019) .
- [42] Pogna, E. A. *et al.* Photo-induced bandgap renormalization governs the ultrafast response of single-layer MoS₂. *ACS Nano* **10** (1), 1182–1188 (2016) .
- [43] Yu, H., Wang, Y., Tong, Q., Xu, X. & Yao, W. Anomalous Light Cones and Valley Optical Selection Rules of Interlayer Excitons in Twisted Heterobilayers. *Physical Review Letters* **115** (18), 1–5 (2015) .
- [44] Selig, M. *et al.* Ultrafast dynamics in monolayer transition metal dichalcogenides: Interplay of dark excitons, phonons, and intervalley exchange. *Physical Review Research* **1** (2), 1–6 (2019) .
- [45] Katsch, F., Selig, M., Carmele, A. & Knorr, A. Theory of Exciton–Exciton Interactions in Monolayer Transition Metal Dichalcogenides. *Physica Status Solidi (B) Basic Research* **255** (12), 1–16 (2018) .
- [46] Holler, J. *et al.* Interlayer exciton valley polarization dynamics in large magnetic fields. *Physical Review B* **105** (8), 1–9 (2021) .
- [47] Ovesen, S. *et al.* Interlayer exciton dynamics in van der Waals heterostructures. *Communications Physics* **2** (1), 23 (2019) .
- [48] Thränhardt, A., Kuckenburg, S., Knorr, A., Meier, T. & Koch, S. W. Quantum theory of phonon-assisted exciton formation and luminescence in semiconductor quantum wells. *Physical Review B* **62** (4), 2706–2720 (2000) .

- [49] Bernardi, M., Palummo, M. & Grossman, J. C. Extraordinary Sunlight Absorption and One Nanometer Thick Photovoltaics Using Two-Dimensional Monolayer Materials. *Nano Letters* **13** (8), 3664–3670 (2013) .
- [50] Lee, C.-H. *et al.* Atomically thin p–n junctions with van der Waals heterointerfaces. *Nature Nanotechnology* **9** (9), 676–681 (2014) .
- [51] Furchi, M. M., Pospischil, A., Libisch, F., Burgdörfer, J. & Mueller, T. Photovoltaic effect in an electrically tunable Van der Waals heterojunction. *Nano Letters* **14** (8), 4785–4791 (2014) .
- [52] Cheng, R. *et al.* Electroluminescence and photocurrent generation from atomically sharp WSe₂/MoS₂ heterojunction p-n diodes. *Nano Letters* **14** (10), 5590–5597 (2014) .
- [53] Zhang, K. *et al.* Interlayer Transition and Infrared Photodetection in Atomically Thin Type-II MoTe₂/MoS₂ van der Waals Heterostructures. *ACS Nano* **10** (3), 3852–3858 (2016) .
- [54] Zhu, T. *et al.* Highly mobile charge-transfer excitons in two-dimensional WS₂/tetracene heterostructures. *Science Advances* **4** (1), 1–9 (2018) .
- [55] Jariwala, D., Sangwan, V. K., Lauhon, L. J., Marks, T. J. & Hersam, M. C. Emerging Device Applications for Semiconducting Two-Dimensional Transition Metal Dichalcogenides. *ACS Nano* **8** (2), 1102–1120 (2014) .
- [56] Villa, A. *et al.* Broadly tunable mid-infrared femtosecond pulses directly generated by an optical parametric amplifier. *OSA Continuum* **4** (11), 2837 (2021) .
- [57] Wegener, M., Chemla, D. S., Schmitt-Rink, S. & Schäfer, W. Line shape of time-resolved four-wave mixing. *Physical Review A* **42** (9), 5675–5683 (1990) .
- [58] Fricke, J. Transport Equations Including Many-Particle Correlations for an Arbitrary Quantum System: A General Formalism. *Annals of Physics* **252** (2), 479–498 (1996) .
- [59] Hübner, M. *et al.* Collective Effects of Excitons in Multiple-Quantum-Well Bragg and Anti-Bragg Structures. *Physical Review Letters* **76** (22), 4199–4202 (1996) .
- [60] Knorr, A., Hughes, S., Stroucken, T. & Koch, S. Theory of ultrafast spatio-temporal dynamics in semiconductor heterostructures. *Chemical Physics* **210** (1-2), 27–47 (1996) .
- [61] Malic, E. & Knorr, A. *Graphene and Carbon Nanotubes* (Wiley, 2013).
- [62] Katsch, F., Selig, M. & Knorr, A. Exciton-Scattering-Induced Dephasing in Two-Dimensional Semiconductors. *Physical Review Letters* **124** (25), 257402 (2020) .
- [63] Kormányos, A. *et al.* k.p theory for two-dimensional transition metal dichalcogenide semiconductors. *2D Materials* **2** (2), 022001 (2015) .

Supplementary information. The online version contains supplementary material available including text and figures in sections Extended Methods and Additional Measurements.

Acknowledgments. We are grateful to C. J. Sayers for helpful discussions and acknowledge F. Morabito, C. Trovatiello, A. Genco, S. Sardar and C. D'Andrea for experimental contributions. We would like to thank the IT and data services members of Zuse Institute Berlin for providing the computing infrastructure. S.D.C. acknowledge financial support from MIUR through the PRIN 2017 Programme (Prot. 20172H2SC4). G.C. acknowledge support by the European Union Horizon 2020 Programme under Grant Agreement 881603 Graphene Core 3. X.Y.Z. acknowledges support for sample fabrication by the Materials Science and Engineering Research Center (MRSEC) through NSF grant DMR-2011738. F.S. and A.V. acknowledge support by the European Research Council (ERC) under the European Union's Horizon 2020 research and innovation programme (grant agreement No. 816313). We acknowledge financial support from the Deutsche Forschungsgemeinschaft (DFG) through SFB 951 Project No. 182087777 (M.K., M.S. and A.K.) and Project KN 427/11-1 (H.M. and A.K.) Project No. 420760124.

Additional Information

- Competing interests: The authors declare no competing interests.
- Availability of data and materials: Data pertaining to this work will be made available by request to the corresponding authors.
- Authors' contributions: V.R.P and S.D.C. devised the experimental work. V.R.P., O.D., and A.V. performed the experimental work; V.R.P. and O.D. performed data analysis. H.M., M.K., and B.K. performed the theoretical work. Q.L. prepared and characterized the TMD HS samples. All authors contributed to the interpretation of the results and preparation of the manuscript.

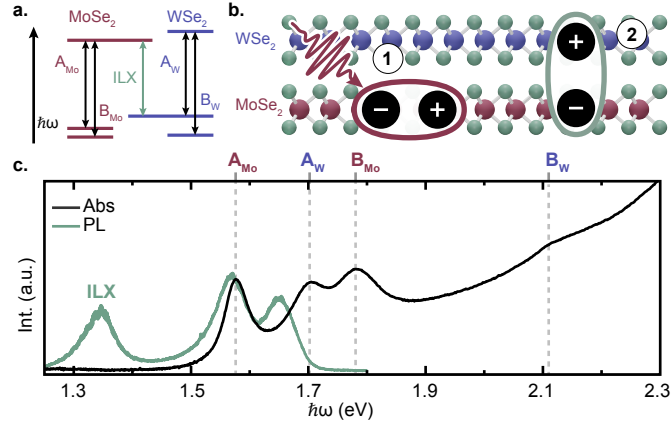


Fig. 1 Interlayer Exciton formation in MoSe₂/WSe₂ HS. **a** Type II band alignment diagram of the MoSe₂/WSe₂ HS. The relevant intralayer and interlayer exciton transitions are depicted with arrows. **b**, ILX formation in the MoSe₂/WSe₂ HS. An intralayer exciton is resonantly excited in the MoSe₂ layer (1). IHT to WSe₂ causes the formation of an optically bright ILX (2). **c**, Linear absorption (black trace) and PL (green trace) spectra of the HS at 77 K. The four peaks in the linear absorption, marked by vertical dashed lines, correspond to A/B intralayer excitons. The PL spectrum reveals a spectral feature below the intralayer exciton absorption edge, which corresponds to the ILX emission peak.

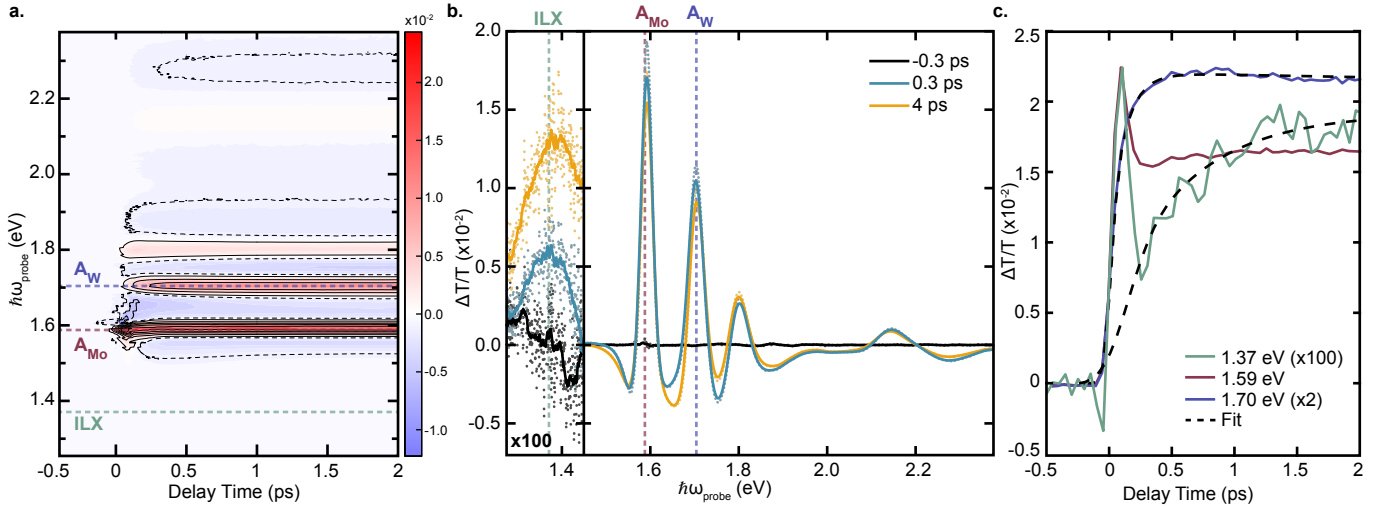


Fig. 2 Transient Optical Response of MoSe₂/WSe₂ HS. **a**, 2D $\Delta T/T$ map as a function of probe energy and delay time. The map displays positive PB (red) and negative PIA signatures (blue) of the intralayer excitons. Dashed lines indicate the probe energy of the three main peaks of interest at A_W (purple), A_{Mo} (red), and the ILX (green). **b**, $\Delta T/T$ spectra from **(a)** at selected early time delays. The region below the intralayer exciton optical gap is multiplied by a factor of 100 to highlight the weak ILX peak in the near IR. **c**, Temporal dynamics of the A_{Mo} (red, $\hbar\omega = 1.59$ eV), A_W (purple, $\hbar\omega = 1.70$ eV), and ILX (green, $\hbar\omega = 1.37$ eV) in the first 2 ps. The A_W and ILX peaks are multiplied by factors of 2 and 100, respectively, to emphasize the delayed rise of these signatures. Dashed lines are the fits to the data.

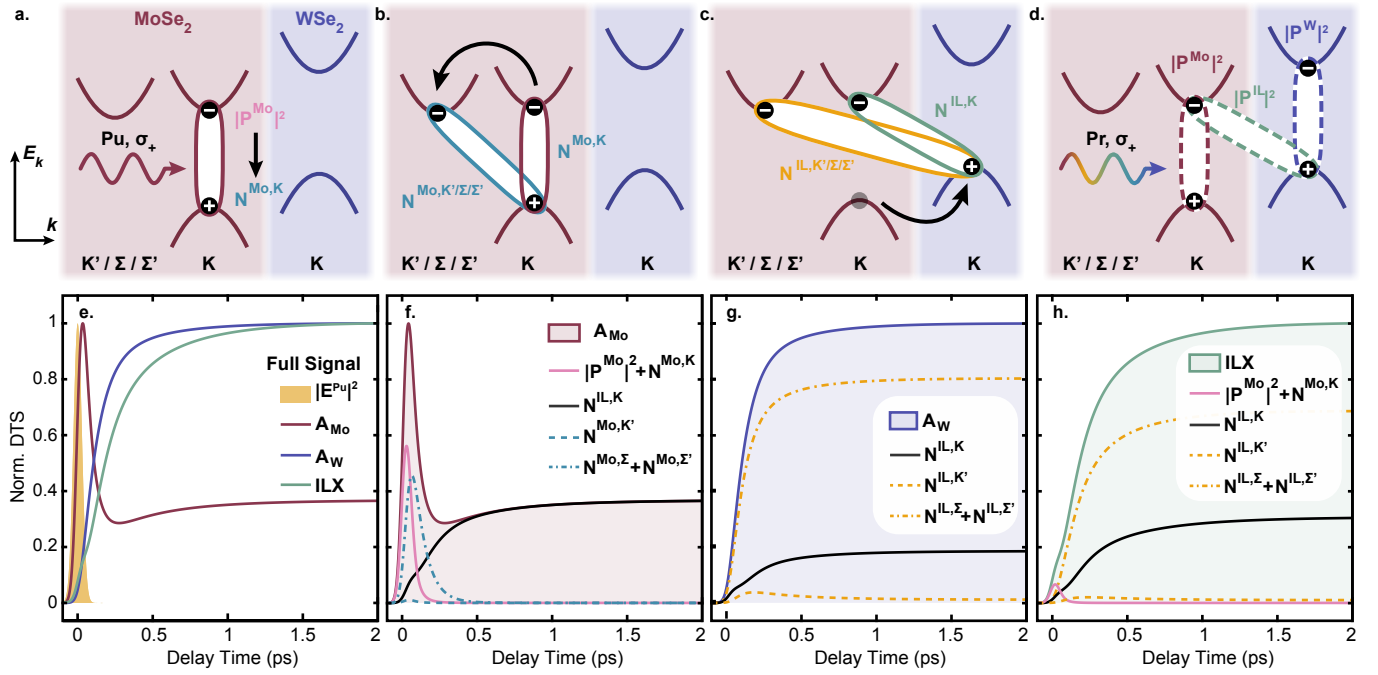


Fig. 3 Sketch of inter- and intra-layer scattering processes and calculated DTS. a-d, Cartoon diagram of interlayer charge transfer and interlayer exciton formation dynamics. MoSe₂ (WSe₂) layer and cartoon bands shown in red (purple). The excitons are represented by full ellipses. a, The A_{Mo} exciton is optically pumped initially generating a coherent polarization, P^{Mo} , and finally the incoherent K-K exciton, $N^{Mo,K}$. b, Subsequent intervalley electron scattering by phonons leads to the formation of intervalley excitonic populations, $N^{Mo,K'/\Sigma/\Sigma'}$. c, Phonon-assisted hole tunneling to the WSe₂ leads to the formation of momentum direct and indirect ILX populations, $N^{IL,K}$ and $N^{IL,K'/\Sigma/\Sigma'}$. Note that the K'/Σ/Σ' valleys are not equivalent. d, The DTS are calculated for the three probed excitonic transitions (dashed ellipses) highlighted in Fig. 2. e, Calculated DTS for the A_{Mo}, A_W and ILX excitons shown in red, purple, and green, respectively, along with the normalized pump pulse in shaded yellow. All the traces are normalized to their maximum. f,g,h, Individual intralayer and interlayer excitonic occupations contributing to the DTS in (e).

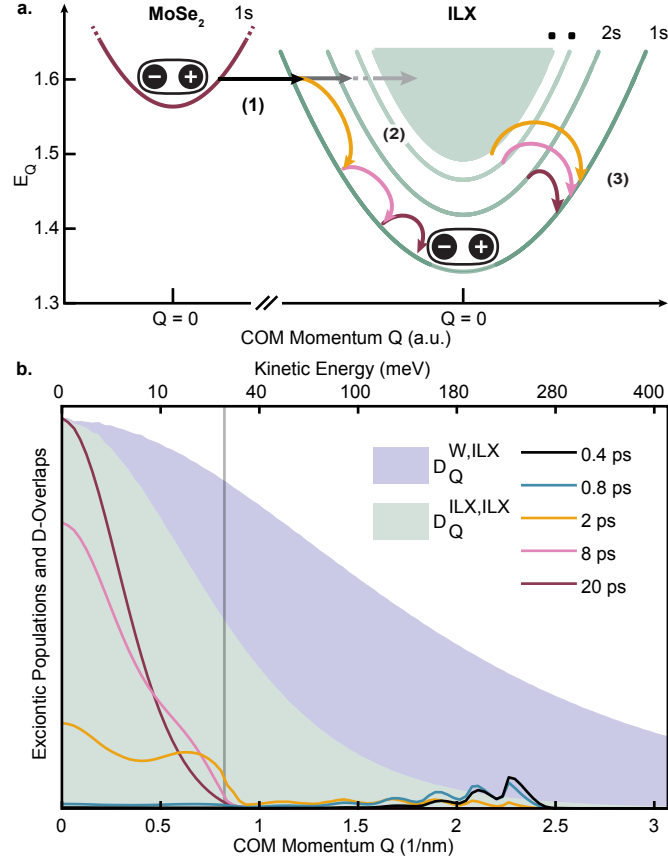


Fig. 4 Hot ILX Relaxation. **a**, Sketch of optically bright ILX formation process following thermal relaxation of hot, momentum dark ILX. The formation process occurs in three steps: (1) After resonant excitation of the A_{Mo} transition, the MoSe₂ layer is populated by incoherent populations, $N_{Q,1s}^{Mo,K}$, (left red parabola) and subsequent phonon-assisted IL hole tunneling leads to the formation of ILX incoherent populations, $N_{Q,\mu}^{IL,K}$, with finite momentum Q and also high quantum number μ (right green parabolas) (see Eq. (1) and Eq. (4)). (2) and (3) The distribution of hot ILX lose energy and momentum by scattering on ultrafast timescales with high energy optical phonons and with low energy acoustic phonons on longer timescales. **b**, Snapshots of the normalized momentum-dependent excitonic populations of ILX at different delays overlaid on the PB weights of the A_W (solid purple) and ILX (solid green) given by Eq. (3). Following IHT, the population distribution of $K-K$ valley ILX, $N_{Q,1s}^{IL,K}$, (lines) is peaked around finite Q values between $2 - 2.5 \text{ nm}^{-1}$, overlapping strongly with A_W . The overlap of the $N_{Q,1s}^{IL,K}$ with the ILX PB weights increases as they shift to lower energy and momentum via scattering processes described in (a). Below the energy threshold of 30 meV (grey line) the scattering is mediated only by acoustic phonons as scattering by optical phonons is energetically forbidden.